Cross sections for proton-induced reactions on Pd isotopes at energies relevant for the γ process

I. Dillmann,* L. Coquard,† C. Domingo-Pardo,‡ F. Käppeler, J. Marganiec,§ and E. Uberseder‖
Karlsruher Institut für Technologie (KIT), Campus Nord, Institut für Kernphysik, Postfach 3640, D-76021 Karlsruhe, Germany

U. Giesen and A. Heiske
Physikalisch-Technische Bundesanstalt (PTB), Bundesallee 100, D-38116 Braunschweig, Germany

G. Feinberg
Soreq Nuclear Research Center, Yavne, Israel

D. Hentschel and S. Hilpp
Karlsruher Institut für Technologie (KIT), Campus Nord, Institut für Nukleare Entsorgung, Postfach 3640, D-76021 Karlsruhe, Germany

H. Leiste
Karlsruher Institut für Technologie (KIT), Campus Nord, Institut für Angewandte Materialien, Postfach 3640, D-76021 Karlsruhe, Germany

T. Rauscher and F.-K. Thielemann
Department of Physics, University of Basel, Klingelbergstrasse 82, CH-4056 Basel, Switzerland
(Received 28 February 2011; published 19 July 2011)

Proton-activation reactions on natural and enriched palladium samples were investigated via the activation technique in the energy range of $E_p = 2.75$–9 MeV, close to the upper end of the respective Gamow window of the γ process. We have determined cross sections for ^{102}Pd$(p,\gamma)^{103}$Ag, ^{104}Pd$(p,\gamma)^{105}$Ag, and ^{105}Pd$(p,n)^{105}$Ag, as well as partial cross sections of ^{104}Pd$(p,n)^{104}$Ag^g, ^{105}Pd$(p,\gamma)^{106}$Ag^m, ^{106}Pd$(p,n)^{106}$Ag^m, and ^{110}Pd$(p,n)^{110}$Ag^m with uncertainties between 3% and 15% for constraining theoretical Hauser-Feshbach rates and for direct use in γ-process calculations.

DOI: 10.1103/PhysRevC.84.015802 PACS number(s): 25.40.−h, 26.30.Ef, 27.60.+j, 97.60.Bw

I. INTRODUCTION

Astrophysical models can explain the origin of most nuclei beyond the iron group as a combination of processes involving neutron captures on long (s process) or short (r process) time scales [1,2]. However, 32 proton-rich stable isotopes between ^{74}Se and ^{196}Hg cannot be formed by these neutron capture reactions because they are either shielded by stable isotopes from the r-process decay chains or lie outside the s-process reaction sequence. These isotopes are attributed to a so-called "p process," and are 10–100 times less abundant than the neighboring s and r nuclei.

The astrophysical details of the p process are still under discussion and it is conceivable that several different nucleosynthesis processes and sites may conspire to produce all of the p nuclei. The currently favored astrophysical site is explosive burning in core collapse supernovae, where a shock front heats the O/Ne shell of the progenitor star to temperatures of 2–3 GK, causing photodisintegration of preexisting seed nuclei [3–6]. The seed nuclei are partly already present in the protostellar cloud from which the star formed and are partly created in a weak s process during hydrostatic burning preceding the explosion. The very rare p nuclei ^{138}La and ^{180}Ta^m cannot be made in this manner, but rather originate from neutrino-induced reactions (ν process [7,8]).

Such a synthesis of proton-rich nuclei by sequences of photodissociations and β^+ decays is also termed the "γ process" [3,6]. The reaction sequences start with (γ, n) reactions at stability, producing proton-richer, unstable nuclei which, in turn, are further disintegrated. When (γ, p) and (γ, α) reactions become comparable to or faster than neutron emission within an isotopic chain, the reaction path is deflected and feeds chains with a lower charge number Z. The decrease in temperature at the later stages of the p process leads to freeze-out via neutron captures and β^+ decays, resulting in the typical p-process abundance pattern with maxima at ^{92}Mo ($N = 50$) and ^{144}Sm ($N = 82$).

Calculations based on the γ-process concept can produce the bulk of the p nuclei [5,6,9]. However, the most abundant p isotopes, ^{92,94}Mo and ^{96,98}Ru, as well as the whole region $A < 124$ are notoriously underproduced. Additionally, the mass region $150 \leqslant A \leqslant 165$ also seems underproduced in modern, self-consistent models [6,10]. It is not yet clear

*Present address: II. Physikalisches Institut, Justus-Liebig-Universität Giessen, and GSI Helmholtzzentrum für Schwerionenforschung GmbH, Darmstadt, Germany; i.dillmann@gsi.de
†Present address: Institut für Kernphysik, Technische Universität Darmstadt, Germany.
‡Present address: Instituto de Fisica Corpuscular (IFIC), E-46071 Valencia, Spain.
§Present address: ExtreMe Matter Institute EMMI, GSI Helmholtzzentrum für Schwerionenforschung GmbH, Darmstadt, Germany.
‖Present address: University of Notre Dame, 225 Nieuwland Science Hall, Notre Dame, IN 46556.

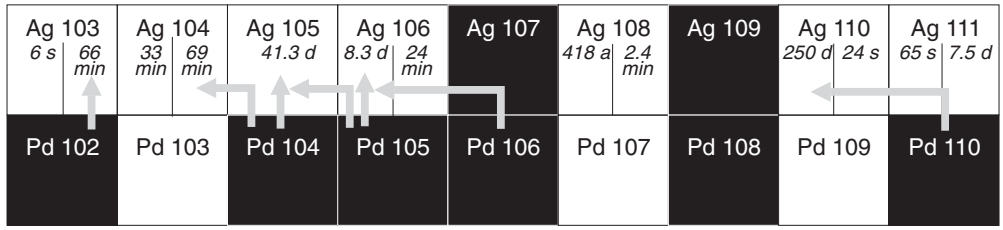

FIG. 1. Isotopic chains of Pd and Ag with the investigated reactions.

whether the observed underproductions are due to deficiencies in the astrophysical modeling or in the nuclear physics input. The lack of seed nuclei for the production of the light p nuclei indicates the former for the lighter mass region, but reliable nuclear physics input is important in both regions. Alternatives to the core-collapse supernova scenario (e.g., explosion of a mass-accreting white dwarf [11] or sub-Chandrasekhar mass white dwarf [12], rapid proton captures in x-ray bursts [13,14], and in the νp process [15]) still suffer from insufficient modeling, constraints from meteoritic data [16], and their uncertain contribution to the total galactic nucleosynthesis. In any case, reliable reaction rates are instrumental for developing a consistent p-process picture.

From the mere size of the nuclear reaction network for the p process, which includes ∼1800 isotopes and more than 10 000 reactions, mostly with unstable nuclei, it becomes obvious that the vast majority of reaction rates has to be determined theoretically.

The experimental database for the p process is—despite many efforts in the past years–still very limited, because measurements of the small cross sections of charged-particle reactions below the Coulomb barrier represent a continuing experimental challenge. In this paper we present the results of (p,γ) and (p,n) reaction studies on several Pd isotopes (as indicated in Fig. 1) close to the astrophysically relevant energies of the p process [17].

The importance of the measured (p,γ) reactions for the p process is twofold. First, theoretical predictions for their cross sections can be tested in order to improve the nuclear reaction modeling for the γ process. Second, reaction rates derived from the measurements can be included directly in the reaction networks for p nucleosynthesis.

The deflections in the γ-process path are governed by (γ,p) reactions in the lighter mass range [18]. Although the (γ,p) rate will dominate over (p,γ) in the γ process, it has been shown that it is always more advantageous to measure the capture rate and derive its inverse rate by application of a detailed balance [19,20]. This is because the reaction rate has to include the thermal population of excited target states in the astrophysical plasma, which leads to cross-section modifications relative to the cross section of the reaction proceeding only via the ground state of a target nucleus. Since only the latter can be studied in the laboratory, it is desirable to measure in the direction of least alteration due to stellar plasma effects. The stellar enhancement factor $\mathrm{SEF} = r^*/r^{\mathrm{lab}}$ is defined as the ratio of the stellar rate r^*, including reactions from thermally populated states of the target nucleus, and the laboratory rate r^{lab} with reactions proceeding only from the ground state of the target nucleus [21]. For the p process, the SEF is always smaller for capture than for photodisintegration [20,22].

The importance of (n,p) reactions for the lower mass range of p nuclei has been pointed out in Ref. [23]. For proton-rich nuclei, (n,p) reactions have a positive reaction Q value and are in general less affected by stellar plasma effects than (p,n) reactions. However, it was pointed out recently that the stellar cross-section modification can be suppressed by the Coulomb barrier and that the SEF may be lower for some (p,n) reactions than for their (n,p) counterpart [19,20]. The reaction $^{105}\mathrm{Pd}(p,n)^{105}\mathrm{Ag}$ is such a case among the reactions presented here. Its SEFs are only 1.1–1.0 in the relevant plasma temperature range of 2.0–3.5 GK, compared to SEFs of 1.3–2.7 for its inverse reaction. For the other (p,n) reactions presented in this paper, we could only determine partial cross sections to the ground or isomeric state. These cannot be directly converted to astrophysical reaction rates but can be used—with the aid of theoretical calculations—to test the description of the proton optical potential, which is also essential in the prediction of the capture and photodisintegration rates.

We commence by describing the experimental technique and sample preparation in Sec. II, followed by the data analysis (Sec. III), and the experimental results in Sec. IV.

II. EXPERIMENTAL TECHNIQUE

All cross-section measurements have been carried out at the cyclotron and Van de Graaff accelerator of Physikalisch-Technische Bundesanstalt (PTB) in Braunschweig, Germany [24] with the activation technique by irradiation of thin sample layers and subsequent counting of the induced activity. The Van de Graaff accelerator was used for energies up to 3.5 MeV, and above that energy up to 9.0 MeV the cyclotron was used. The astrophysically relevant energy ranges for the measured reactions at temperatures of 2 and 3 GK are listed in Table I. In most of the measurements, our data reaches into the energy window relevant in the γ process.

A. Sample preparation

Samples of natural composition were prepared by sputtering ≈400-nm-thick layers of Pd metal onto 1-mm-thick Al disks that are 35 mm in diameter. Enriched ^{104}Pd and ^{105}Pd samples (from STB Isotopes, Germany, Table II) were first produced by electrodeposition of a $PdCl_2$ solution on tantalum backings (see Ref. [25] for a sketch of the electrolysis cell), but

TABLE I. Astrophysically relevant energy windows for the measured ^{A}Pd(p,γ) and ^{A}Pd(p,n) reactions at 2 and 3 GK [17]. Values in parentheses refer to the range at 3 GK. The last column shows the measured energy range.

Reaction	T (GK)	Lower end (MeV)	Upper end (MeV)	Measured (MeV)
^{102}Pd(p,γ)	2 (3)	1.64 (2.04)	3.30 (4.29)	2.68–6.85
^{104}Pd(p,γ)	2 (3)	1.67 (2.13)	3.40 (4.45)	2.69–5.04
^{105}Pd(p,γ)	2 (3)	1.51 (1.74)	2.81 (3.90)	2.71−5.04
^{104}Pd(p,n)	2 (3)	5.07 (5.07)	5.70 (6.07)	5.80–8.82
^{105}Pd(p,n)	2 (3)	3.87 (4.24)	5.50 (5.98)	2.69–5.04
^{106}Pd(p,n)	2 (3)	3.75 (3.76)	4.35 (4.69)	3.18–4.91
^{110}Pd(p,n)	2 (3)	1.71 (1.80)	2.92 (3.74)	3.43–8.81

these layers did not properly adhere to the backings. Instead, the samples were made by careful and uniform deposition of 100 μl of the $PdCl_2$ solution within the area of the beam spot (12 mm in diameter) and subsequent drying.

The thicknesses of the Pd samples were determined by x-ray fluorescence (XRF) by irradiation of the samples with the bremsstrahlung spectrum of a rhodium anode. The induced characteristic Pd x rays were analyzed by reflection on a LiF crystal. This setup was calibrated relative to a blank sample and to six Pd reference samples (50–500 μg) prepared from a standard solution.

The natural samples were between 420 and 520 nm in thickness, corresponding to a Pd mass of (395–490) μg or (2.9–3.6) $\times 10^{18}$ atoms/cm^2. The enriched samples were approximately twice as thick and contained (680–850) μg or (3.4–4.2) $\times 10^{18}$ atoms/cm^2 of ^{104}Pd or ^{105}Pd.

B. Experimental setup

The samples were irradiated in an activation chamber, which was designed as a Faraday cup (Fig. 2). The charge deposited on the sample was recorded in short time steps by a current integrator for offline correction of beam fluctuations (which turned out to be negligible in the end).

The proton beam was wobbled across the chamber aperture indicated in Fig. 2 for homogeneous illumination of the Pd samples. The aperture was slightly smaller than the negatively charged diaphragm ($U_S = -300$ V) for suppression

TABLE II. Mass fractions (in percent) of the natural [26] and enriched samples.

	Natural sample	Enriched sample	
		^{104}Pd	^{105}Pd
^{102}Pd	1.02(1)	0.10(2)	0.01(2)
^{104}Pd	11.14(8)	97.0(1)	0.32(10)
^{105}Pd	22.33(8)	2.30(5)	94.50(5)
^{106}Pd	27.33(3)	0.45(5)	4.59(5)
^{108}Pd	26.46(9)	0.10(2)	0.46(2)
^{110}Pd	11.72(9)	0.05	0.13

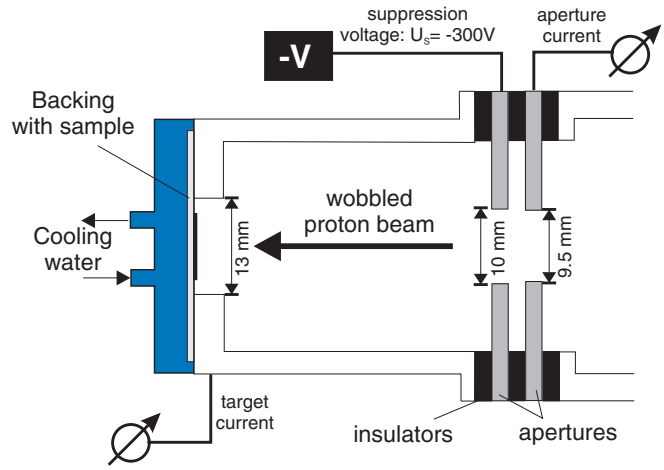

FIG. 2. (Color online) Experimental setup at the PTB beamline.

of secondary electrons. The samples with the Pd layers were water cooled from the outside. For each energy step the proton-beam spot was adjusted by means of a quartz window to ensure that the sample was completely illuminated. The beam energy was defined within an uncertainty of ±25 keV by means of field calibration of two analyzing magnets as well as by a time-of-flight measurement of the particle velocity [27]. At energies below 3.5 MeV the Van de Graaff accelerator was used, where the uncertainty of the beam energy calibration was less than 3 keV.

For each activation the effective proton energy was determined according to Eq. (4.99) in Ref. [21],

$$E_p^{\text{eff}} = E_{\text{c.m.}} - \Delta + \Delta\left(- \frac{\sigma_2}{\sigma_1 - \sigma_2} + \left[\frac{\sigma_1^2 + \sigma_2^2}{2(\sigma_1 - \sigma_2)^2} \right]^{1/2} \right), \tag{1}$$

where Δ is the target thickness (energy loss) calculated with the Monte Carlo program SRIM 2003 [28], $E_{\text{c.m.}}$ is the respective center-of-mass energy, and σ_1,σ_2 are the measured cross sections of two neighboring points. As can be seen from Eq. (1), the error bars of E^{eff} become asymmetric, with the smaller component in a positive direction due to the correction factor in brackets.

The samples were activated at 16 different proton energies between 2.75 and 9.00 MeV, switching between short-time activations (up to 7200 s for the 65.7-min ground state in ^{103}Ag) and long-time activations (up to 36 000 s at 2.75 MeV). The average beam current was 10 μA for the natural samples and 5 μA for the enriched samples.

The produced activity was measured offline with two different HPGe detectors (efficiency curves in Fig. 3), which were shielded from room background by 10-cm lead. The efficiencies shown in Fig. 3 were determined with an uncertainty of 2% by a set of calibrated reference sources. Apart from the 64-keV transition in ^{105}Ag, which is very close to the calibration point at 60 keV measured with an ^{241}Am source, all analyzed γ-ray lines are in the well-defined part of the efficiency curves above 100 keV (Table III).

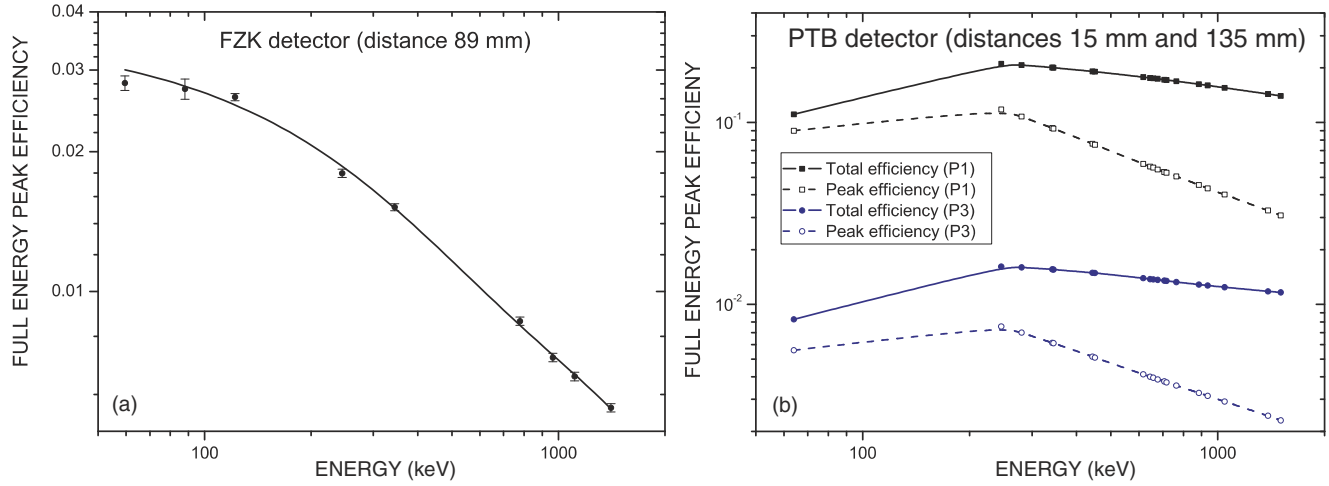

FIG. 3. Efficiency curves of the two HPGe detectors: (a) FZK detector, (b) PTB detector. The measured efficiency values of the PTB detector are connected with lines to guide the eye.

III. DATA ANALYSIS

The total amount of activated nuclei N_a at the end of the irradiation can be deduced from the number of events C in a particular γ-ray line (Table III) registered in the HPGe detector during the measuring time t_m [29]:

$$N_a = \frac{C(t_m)}{S\varepsilon_\gamma I_\gamma (1 - e^{-\lambda t_m}) e^{-\lambda t_w}}. \quad (2)$$

TABLE III. Decay properties of the product nuclei [30–34]. Shown here are only transitions used for analysis.

Isotope	$t_{1/2}$	E_γ (keV)	I_γ (%)
^{103}Ag^{g+m}	65.7 (7) min	118.7	31.2(7)
		148.2	28.3(5)
		243.9	8.5(5)
		266.9	13.4(4)
		1273.8	9.4(3)
^{104}Ag^{g}	69.2 (7) min	740.5	7.2(9)[a]
		758.7	6.4(8)[a]
		767.6	65.7(21)
		942.6	25.0(23)[a]
		1625.8	5.1(7)[a]
^{105}Ag^{g}	41.29 (7) d	64.0	10.5(10)
		280.4	30.2(17)
		344.5	41.4(6)
		443.4	10.5(5)
^{106}Ag^{m}	8.28 (2) d	451.0	28.2(7)
		717.2	28.9(8)
		748.4	20.6(6)
		1045.8	29.6(10)
^{110}Ag^{m}	249.76 (4) d	657.8	94.3(3)
		763.9	22.62(21)
		884.7	72.7(4)
		937.5	34.2(6)

[a]New intensities—see Table V.

The factor t_w corresponds to the waiting time between irradiation and activity measurement. The factors ε_γ and I_γ account for the HPGe efficiency and the relative γ intensity per decay (Table III) of the respective transition, and S is the correction factor for coincidence summing.

Throughout the activations the proton flux was recorded in time steps of 1 min, but time variations were found to be negligible. Therefore, the correction for the decay during activation f_b could be calculated by the expression for constant flux, $f_b = \frac{1-\exp(-\lambda t_a)}{\lambda t_a}$. Any γ-ray self-absorption is negligible due to the thin Pd layers. The cross section (in barn) at the respective proton energy can then be calculated via

$$\sigma(E_p) = \frac{N_a \lambda t_a 10^{24}}{H N \Phi_{\text{tot}} (1 - e^{-\lambda t_a})}. \quad (3)$$

H is the abundance of the respective Pd isotope (Table II), Φ_{tot} is the collected proton charge during the activation time t_a, and λ is the decay constant. N is the area density of the Pd samples in cm^{-2}.

A. Coincidence-summing corrections

Coincidence summing occurs when two or more γ rays are recorded within the resolving time of the detector [35]. The induced activities were measured with two different HPGe detectors (labeled "FZK detector" and "PTB detector" in Fig. 3). The FZK detector is an n-type coaxial detector with a thin carbon window and a crystal volume of 370 cm^3 corresponding to a relative efficiency of 100%. The PTB detector is a p-type coaxial detector with an aluminum window and a crystal volume of 300 cm^3 corresponding to a relative efficiency of 70%. All efficiencies are given with respect to 3 in. × 3 in. NaI(Tl) detectors.

Because the FZK detector was only used for measurements at a distance of 89 mm, the summing corrections are low and were estimated with one sample measured also at a larger distance of 164 mm. The respective results were in perfect agreement with the calculated summing corrections. For the

TABLE IV. Relative uncertainties for the individual measurements in percent. Values in parentheses refer to enriched samples.

Source of uncertainty	^{102}Pd(p,γ) $\rightarrow^{103}$Ag	^{104}Pd(p,n) $\rightarrow^{104}$Ag^{g}	^{104}Pd(p,γ) $\rightarrow^{105}$Ag	^{105}Pd(p,γ) $\rightarrow^{106}$Ag^{m}	^{105}Pd(p,n) $\rightarrow^{105}$Ag	^{106}Pd(p,n) $\rightarrow^{106}$Ag^{m}	^{110}Pd(p,n) $\rightarrow^{110}$Ag^{m}
Isotopic abundance	0.98	0.72 (0.10)		0.36 (0.05)		0.11	0.77
Detector efficiency				2.0			
Beam current integration				1.0			
Sample mass (XRF)				1.5			
γ-ray intensity	1.8–5.9	3.2–4.3	1.5–9.5	2.5–3.4	1.5–9.5	2.5–3.4	0.3–1.8
Statistical error	2.5–15	0.3–0.6	0.2–7.7	3.0–19	0.2–3.6	3.0–12	0.7–14
Total uncertainty	4.1–16	4.8–5.1	3.0–13	4.7–19	3.0–11.0	4.7–13	2.7–14

PTB detector, which was used at two distances (P1 = 15 mm and P3 = 135 mm) total and peak efficiencies were available from previous experiments (Fig. 3) and could be used for the calculation of coincidence-summing corrections. In this work, summing corrections are significant only for measurements with the PTB detector at the short distance P1, which had to be used for the runs at the lowest energies.

B. Uncertainties

The systematic and statistical uncertainties from these measurements are summarized in Table IV. The energy loss of the proton beam in the Pd layer was calculated with SRIM 2003 [28] using the optional tables for range and stopping power. A sample thickness of typically 460 nm corresponds to an average energy loss between 30 keV at 2.5 MeV and 15 keV at 9 MeV proton energy. The respective uncertainty of the proton energy is 25 keV for the cyclotron and $\leqslant$3 keV for the Van de Graaff accelerator. As shown in Eq. (1), the error bars of E_p^{eff} are asymmetric, with the smaller component in the positive direction. The uncertainty in the collection of the proton beam current was determined to be $\leqslant$1%.

The emission probabilities of the γ transitions in the decay of ^{104}Ag^{g} exhibit rather large uncertainties (see Table III). Some of these uncertainties could be reduced by factors of 3 by normalization to the strongest transition at 767.6 keV. The previous and improved intensities are compared in Table V.

At the lower part of the investigated energy range the total uncertainties are dominated by poor counting statistics, except for cases with a favorable half-life, which could be counted for longer times (e.g., ^{105}Ag). The systematic uncertainties are composed of the contributions from the detection efficiencies (2%), the XRF measurement of the sample mass (1.5%), the integrated proton charge (1%), the γ-ray intensities (Table III), and the isotopic abundances (Table II) [26].

TABLE V. Improved γ-ray intensities (in %) for the decay of ^{104}Ag^{g}.

E_γ (keV)	I_γ [31]	I_γ (new)
740.5	7.2(9)	7.19(31)
758.7	6.4(8)	6.62(26)
767.6	65.7(21)	65.7(21)
942.6	25.0(23)	23.69(83)
1625.8	5.1(7)	5.25(19)

IV. RESULTS

In the following, we present our results for each of the reactions individually and compare them to literature data and to published predictions of the NON-SMOKER code [36,37]. As already explained in Sec. I, (p,γ) and (p,n) reactions and their inverses are directly important in the γ process. However, they occur at lower reaction energies than were accessible experimentally. Nevertheless, the data may be compared to theoretical predictions to pinpoint possible systematic problems in the predictions or their input data, which also may play a role at lower energies. In this respect, (p,γ) and (p,n) reactions contribute different types of information for the treatment of the optical potentials and γ strengths. On the one hand, the (p,n) reactions are most sensitive to the proton strength functions, and thus to the proton optical potential, across almost the total range of measured energies, provided that the averaged neutron widths are dominating the total reaction width. This is the case for energies well above the threshold. A few hundreds of keV above the threshold, neutron widths may be comparable to γ and proton widths and the cross section will be sensitive to variations in either of them. On the other hand, depending on the target nucleus, proton capture is more sensitive to the γ strengths at higher energies, whereas it has a higher sensitivity to the proton optical potential at low energies, where the averaged proton widths become smaller than the averaged γ widths. Therefore, an interpretation of possible deviations of theory from experiment has to consider the relative importance of the different nuclear properties at each energy.

The total cross sections for ^{102}Pd$(p,\gamma)^{103}$Ag, ^{104}Pd$(p,\gamma)^{105}$Ag, and ^{105}Pd$(p,n)^{105}$Ag have been measured in the proton energy range between 2.75 and 9.00 MeV. These results could be complemented by the partial cross sections for ^{104}Pd$(p,n)^{104}$Ag^{g}, ^{105}Pd$(p,\gamma)^{106}$Ag^{m}, ^{106}Pd$(p,n)^{106}$Ag^{m}, and ^{110}Pd$(p,n)^{110}$Ag^{m}.

A. ^{102}Pd$(p,\gamma)^{103}$Ag

The total proton capture cross section of ^{102}Pd was determined via five γ transitions at 118.7, 148.2, 243.9, 266.9, and 1273.8 keV. The half-life of ^{103}Ag was also checked and yielded 68.2 $\pm$ 2.4 min, slightly longer than but still consistent

TABLE VI. Cross sections and S factors for ^{102}Pd$(p,\gamma)^{103}$Ag.

E^{eff} (MeV)	Cross section (mb)	S factor (10^7 MeV b)
$2.685^{+0.013}_{-0.018}$	0.058 ± 0.010	15.7 ± 2.8
$2.932^{+0.012}_{-0.018}$	0.105 ± 0.016	9.50 ± 1.4
$3.178^{+0.012}_{-0.016}$	0.266 ± 0.028	9.16 ± 0.95
$3.422^{+0.012}_{-0.015}$	0.522 ± 0.046	7.69 ± 0.68
$3.679^{+0.025}_{-0.029}$	0.797 ± 0.070	5.29 ± 0.47
$3.894^{+0.026}_{-0.029}$	1.43 ± 0.11	5.19 ± 0.41
$3.934^{+0.026}_{-0.029}$	1.42 ± 0.12	4.62 ± 0.37
$4.169^{+0.027}_{-0.028}$	2.12 ± 0.18	3.80 ± 0.32
$4.369^{+0.028}_{-0.029}$	2.60 ± 0.18	2.93 ± 0.20
$4.435^{+0.028}_{-0.030}$	3.06 ± 0.23	2.98 ± 0.22
$4.889^{+0.030}_{-0.030}$	5.08 ± 0.38	1.96 ± 0.15
$4.912^{+0.028}_{-0.032}$	5.26 ± 0.43	1.94 ± 0.16
$5.800^{+0.031}_{-0.033}$	12.3 ± 1.0	1.05 ± 0.09
$6.851^{+0.035}_{-0.037}$	10.6 ± 2.0	0.24 ± 0.04

with 65.7 ± 0.7 min given in Ref. [30]. The cross sections (derived as weighted averages from all five transitions) are listed in Table VI, together with the respective S factors.

The present results are compared in Fig. 4 with the previous data of Özkan *et al.* [38] and with NON-SMOKER predictions [36,37]. The typical factor-of-2 uncertainty of this prediction for proton-capture reactions is indicated by the gray band. Within these limits there is rather good agreement with this measurement, although the NON-SMOKER values show a somewhat different energy dependence.

The present results are approximately a factor of 3 lower than the experimental data of Özkan *et al.* [38]. These authors used enriched ^{102}Pd samples with an area density of 2 mg/cm^2, three times thicker than in this work. This explains the larger energy spread of the data points (60–90 keV) but does not explain the discrepancy between both measurements.

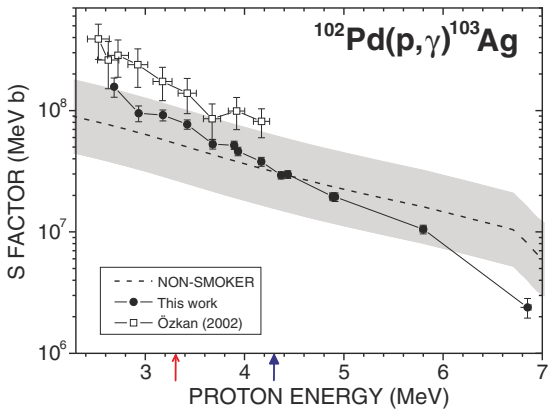

FIG. 4. (Color online) S factors for ^{102}Pd$(p,\gamma)^{103}$Ag. The predictions from NON-SMOKER [36,37] (dashed line) are plotted with a region of uncertainty of a factor of 2. The comparison with the ^{102}Pd$(p,\gamma)^{103}$Ag results of Özkan *et al.* [38] (open symbols) exhibits a clear discrepancy. The thin and thick arrows indicate the upper ends of the respective Gamow windows for $T = 2$ and 3 GK, respectively (see Table I).

We have to distinguish three different regions in the energy range studied here. At the lower end up to an energy of ~4.5 MeV the cross-section predictions are mostly sensitive to the predicted averaged proton width. Above that energy, the proton width becomes larger than the γ width and consequently the sensitivity to the latter dominates. The data point at the highest energy is closely above the (p,n) threshold, and the neutron width will have an additional impact there. It can be seen that the energy dependence of the cross section is slightly different in the three different regimes (this is more pronounced in the data) because it is given by the energy dependence of different nuclear properties. Since the proton widths are most important at p-process energies, we focus on the lowest energies. The data is higher than the prediction at these energies but it is difficult to identify a trend because of the increasing impact of the γ width toward higher energy. The experimental results lie within the expected theoretical uncertainty of a factor of 2 and are compatible with the assumption that the theoretical proton widths just have to be scaled by a constant factor.

B. ^{104}Pd$(p,n)^{104}$Ag^g

The ^{104}Pd$(p,n)^{104}$Ag reaction channel opens at $E_p = 5.11$ MeV. The 5^+ ground state ($t_{1/2} = 69.2$ min) and the 2^+ isomeric state ($t_{1/2} = 33.5$ min) of ^{104}Ag are decaying both via β^+ decay and electron capture (EC) and are not directly connected by internal decay. The shorter half-life of the isomer made it difficult to derive the isomeric cross section. Therefore, only the cross section to the ground state was determined after an appropriate waiting time. To avoid interferences, the analysis was limited to those γ transitions, where feeding from the isomer is excluded or negligibly weak, i.e., the γ lines at 740.5, 758.7, 767.6, 942.6, and 1625.8 keV. The weighted cross sections and the S factors are summarized in Table VII.

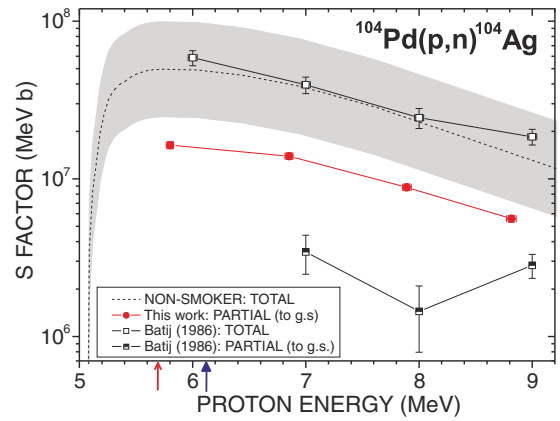

FIG. 5. (Color online) S factors for ^{104}Pd$(p,n)^{104}$Ag. The predictions from NON-SMOKER [36,37] (dashed line) are plotted with a region of uncertainty of a factor of 2. For ^{104}Pd$(p,n)^{104}$Ag the present results are compared to the measurement of Batij *et al.* [39]. The thin and thick arrows indicate the upper ends of the respective Gamow windows for $T = 2$ and 3 GK, respectively (see Table I).

TABLE VII. Partial cross sections and S factors for ^{104}Pd$(p,n)^{104}$Ag^g.

E^{eff} (MeV)	Cross section (mb)	S factor (10^7 MeV b)
$5.802^{+0.030}_{-0.035}$	19.2 ± 1.0	1.64 ± 0.08
$6.852^{+0.035}_{-0.037}$	62.1 ± 3.0	1.40 ± 0.07
$7.892^{+0.039}_{-0.040}$	111.3 ± 5.4	0.88 ± 0.04
$8.815^{+0.042}_{-0.043}$	149.9 ± 7.4	0.56 ± 0.03

The comparison in Fig. 5 shows significant discrepancies with the partial cross sections reported by Batij *et al.* [39]. Since NON-SMOKER results are not available for the partial cross section, the total cross section is plotted instead. In spite of the puzzling partial cross sections, the total cross sections of Ref. [39] are in good agreement with the theoretical result, confirming the averaged proton widths obtained by using the optical potential of Ref. [40] for this energy range. The present (partial) cross section exhibits the same trend as the NON-SMOKER curve.

Following the EXFOR database [41], the data from Bitao *et al.* [42] is listed as the ratio of isomeric to ground-state cross section, $X = \frac{\sigma_m}{\sigma_g}$. These ratios were deduced via the transitions at 556, 768, and 1239 keV occurring in the decay of the isomer as well as of the ground state. Using our experimental data and the total cross section from Ref. [39], we also deduced the ratio X, yielding values between 3.7 for 5.802 MeV and 2.8 for 8.815 MeV, in clear disagreement with the values of $X = 0.031$–0.132 for energies between 6.31 and 8.99 MeV given in Ref. [42]. Unfortunately, these authors do not give any information on how their ratios were calculated nor on the cross-section data used.

TABLE VIII. Composite cross section and S factor for the ^{104}Pd$(p,\gamma) + {}^{105}$Pd(p,n) reactions.

E^{eff}	Measured data [^{104}Pd$(p,\gamma) + {}^{105}$Pd(p,n)]	
	σ^+	S^+ factor
(MeV)	(mb)	(10^8 MeV b)
$2.687^{+0.012}_{-0.019}$	0.073 ± 0.005	1.96 ± 0.14
$2.933^{+0.012}_{-0.018}$	0.185 ± 0.013	1.67 ± 0.12
$3.178^{+0.012}_{-0.016}$	0.47 ± 0.03	1.61 ± 0.11
$3.424^{+0.013}_{-0.014}$	0.92 ± 0.07	1.35 ± 0.10
$3.444^{+0.013}_{-0.014}$	1.11 ± 0.08	1.52 ± 0.12
$3.679^{+0.025}_{-0.029}$	1.96 ± 0.14	1.30 ± 0.09
$3.894^{+0.026}_{-0.029}$	3.69 ± 0.24	1.34 ± 0.09
$3.934^{+0.027}_{-0.028}$	3.82 ± 0.27	1.24 ± 0.09
$4.170^{+0.026}_{-0.029}$	6.47 ± 0.43	1.16 ± 0.08
$4.436^{+0.027}_{-0.031}$	8.49 ± 0.60	0.95 ± 0.07
$4.890^{+0.028}_{-0.031}$	20.5 ± 1.5	0.79 ± 0.06
$4.912^{+0.029}_{-0.031}$	21.6 ± 1.6	0.80 ± 0.06

TABLE IX. Cross sections and S factors for ^{104}Pd$(p,\gamma)^{105}$Ag from enriched samples.

E^{eff} (MeV)	Cross section (mb)	S factor (10^7 MeV b)
$2.714^{+0.010}_{-0.017}$	0.024 ± 0.003	5.75 ± 0.74
$2.963^{+0.009}_{-0.014}$	0.091 ± 0.011	7.24 ± 0.89
$3.653^{+0.023}_{-0.028}$	0.634 ± 0.047	4.54 ± 0.34
$3.991^{+0.024}_{-0.028}$	1.654 ± 0.124	4.64 ± 0.32
$4.473^{+0.026}_{-0.029}$	3.640 ± 0.214	3.27 ± 0.19
$5.035^{+0.027}_{-0.031}$	6.104 ± 0.394	1.80 ± 0.12

C. ^{104}Pd$(p,\gamma)^{105}$Ag and ^{105}Pd$(p,n)^{105}$Ag

1. *Cross sections measured with natural samples*

Because the ^{104}Pd$(p,\gamma)^{105}$Ag and ^{105}Pd$(p,n)^{105}$Ag reactions are leading to the same product nucleus, only the sum of the two cross sections can be determined above the (p,n) threshold at 2.15 MeV. This composite cross section,

$$\sigma^+(N_{104} + N_{105}) = N_{104}\sigma_{pg} + N_{105}\sigma_{pn}, \tag{4}$$

was determined using the γ transitions at 64.0, 280.4, 344.5, and 443.4 keV. The 7.23-min isomer in ^{105}Ag could not be resolved due to its short half-life, but this state decays by 99.66% via internal transitions. Therefore, the 0.34% electron capture branch has a negligible effect on the total cross section. The results are shown in Table VIII.

2. *^{104}Pd$(p,\gamma)^{105}$Ag measured with enriched samples*

The total ^{104}Pd$(p,\gamma)^{105}$Ag cross section was measured additionally with enriched ^{104}Pd samples (Table IX). In Fig. 6 our results are compared to the values of Ref. [43], which are in very good agreement with the NON-SMOKER predictions. Our results are slightly lower, but follow the theoretical and experimental energy trend and—with the exception of the highest data point—reproduce the theoretical values within the factor-of-2 error band.

3. *^{105}Pd$(p,n)^{105}$Ag measured with enriched samples*

The ^{105}Pd$(p,n)^{105}$Ag reaction channel opens at 2.15 MeV. The total cross section could also be measured from enriched

TABLE X. Cross sections and S factors for ^{105}Pd$(p,n)^{105}$Ag from enriched samples.

E^{eff} (MeV)	Cross section (mb)	S factor (10^7 MeV b)
$2.714^{+0.011}_{-0.018}$	0.017 ± 0.002	3.93 ± 0.38
$2.961^{+0.011}_{-0.017}$	0.068 ± 0.006	5.47 ± 0.50
$3.651^{+0.024}_{-0.027}$	0.794 ± 0.052	5.72 ± 0.37
$3.991^{+0.025}_{-0.027}$	1.861 ± 0.122	5.22 ± 0.34
$4.473^{+0.027}_{-0.028}$	4.383 ± 0.279	3.93 ± 0.25
$5.038^{+0.025}_{-0.027}$	7.571 ± 0.410	2.22 ± 0.12

TABLE XI. Composite cross section and S factor for the ^{105}Pd$(p,\gamma)^{106}$Ag^m + ^{106}Pd$(p,n)^{106}$Ag^m reactions. The horizontal line indicates where the ^{106}Pd(p,n) reaction starts to contribute.

E^{eff}(MeV)	Measured data [^{105}Pd(p,γ) + ^{106}Pd(p,n)]	
	σ^+ (μb)	S^+ factor (10^6 MeV b)
$3.178^{+0.013}_{-0.015}$	3.6 ± 0.4	1.233 ± 0.138
$3.424^{+0.011}_{-0.016}$	5.0 ± 0.6	0.735 ± 0.093
$3.444^{+0.024}_{-0.029}$	6.1 ± 0.6	0.838 ± 0.084
$3.679^{+0.026}_{-0.029}$	9.6 ± 1.6	0.640 ± 0.107
$3.894^{+0.028}_{-0.028}$	15.0 ± 1.8	0.546 ± 0.064
$3.937^{+0.025}_{-0.030}$	15.1 ± 2.1	0.488 ± 0.069
$4.170^{+0.027}_{-0.029}$	44.6 ± 4.9	0.802 ± 0.088
$4.370^{+0.028}_{-0.029}$	63.6 ± 8.8	0.718 ± 0.100
$4.438^{+0.025}_{-0.031}$	77.8 ± 5.2	0.753 ± 0.050
$4.890^{+0.030}_{-0.031}$	299 ± 22	1.152 ± 0.083
$4.913^{+0.028}_{-0.031}$	307 ± 25	1.133 ± 0.092

^{105}Pd samples via the above-mentioned γ transitions (Table X). Figure 6 shows these results, which are again slightly lower than the NON-SMOKER prediction. With the exception of the highest data point, our results can reproduce the theoretical values within the factor-of-2 region of uncertainty. Unfortunately there is no other data available for comparison.

D. ^{105}Pd$(p,\gamma)^{106}$Ag^m and ^{106}Pd$(p,n)^{106}$Ag^m

The partial cross section to the ground state in ^{106}Ag was not accessible by the activations because of its short half-life of 23.96 min. The EC decay of the 6^+ isomeric state with $t_{1/2} = 8.28$ d to ^{106}Pd could be followed via the transitions at 451.0, 717.2, 748.4, and 1045.8 keV. Measurements have been performed with natural and with enriched samples (Table II).

TABLE XII. Cross sections and S factors for the ^{105}Pd$(p,\gamma)^{106}$Ag^m reaction measured with enriched samples.

E^{eff} (MeV)	Cross section (μb)	S factor (10^6 MeV b)
$2.714^{+0.011}_{-0.018}$	0.44 ± 0.10	1.063 ± 0.238
$2.961^{+0.011}_{-0.017}$	1.50 ± 0.20	1.202 ± 0.163
$3.462^{+0.006}_{-0.009}$	3.99 ± 0.65	0.518 ± 0.084
$3.651^{+0.024}_{-0.027}$	9.68 ± 1.08	0.699 ± 0.078
$3.991^{+0.025}_{-0.027}$	17.6 ± 1.7	0.495 ± 0.049
$4.473^{+0.027}_{-0.028}$	26.8 ± 2.6	0.240 ± 0.023
$5.038^{+0.025}_{-0.027}$	38.7 ± 4.2	0.114 ± 0.012

1. *Cross sections measured with natural samples*

Above the threshold of the ^{106}Pd(p,n) reaction at 3.78 MeV, the measured cross section represents the composite of the partial cross sections for ^{105}Pd$(p,\gamma)^{106}$Ag^m and ^{106}Pd$(p,n)^{106}$Ag^m, similar to the previous case. The results are listed in Table XI and shown in Fig. 7.

2. *^{105}Pd$(p,\gamma)^{106}$Ag^m measured with enriched samples*

The ^{105}Pd$(p,\gamma)^{106}$Ag^m cross section was also measured with enriched ^{105}Pd samples between $E_p = 2.7$ and 5.0 MeV. The resulting S factor (Table XII) is shown in Fig. 7 and agrees well with the data from the natural samples below the ^{106}Pd(p,n) threshold.

The results obtained with the enriched samples could be used to decompose the cross section data in Table XI to derive the cross section for the competing ^{106}Pd$(p,n)^{106}$Ag^m channel (Table XIII). Our deduced results are compared in Fig. 7 with experimental data of Batij *et al.* [39], which are reported at slightly higher energies. The results of Ref. [39] for the total cross section are higher than the values of Bitao *et al.* [44].

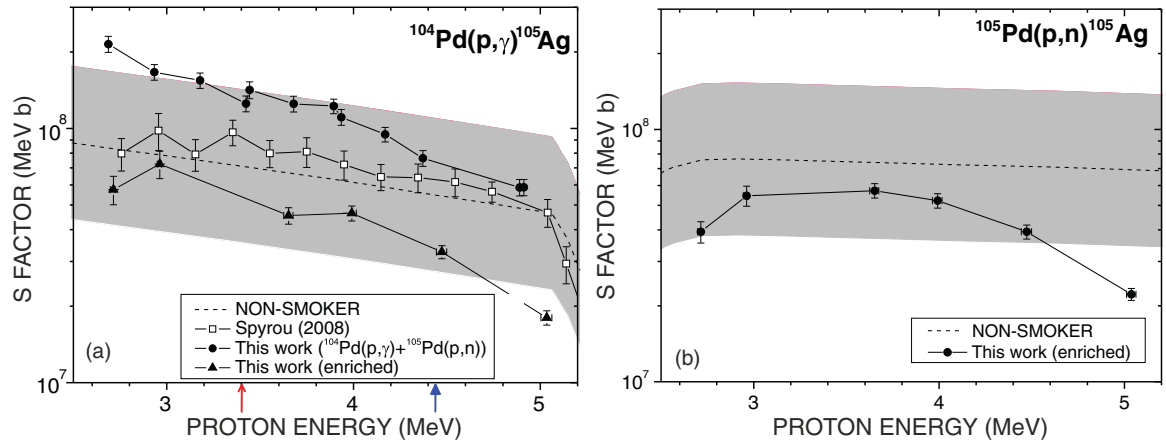

FIG. 6. (Color online) (a) S factors for ^{104}Pd$(p,\gamma)^{105}$Ag. The data from Spyrou [43] is shown in comparison with our composite S factor for ^{104}Pd(p,γ) + ^{105}Pd(p,n) and the results from the enriched samples. (b) S factors for ^{105}Pd$(p,n)^{105}$Ag from the enriched samples. The predictions from NON-SMOKER [36,37] (dashed line) are shown with a region of uncertainty of a factor of 2. The thin and thick arrows indicate the upper ends of the respective Gamow windows for $T = 2$ and 3 GK, respectively. For ^{105}Pd$(p,n)^{105}$Ag the limits are off scale (see Table I).

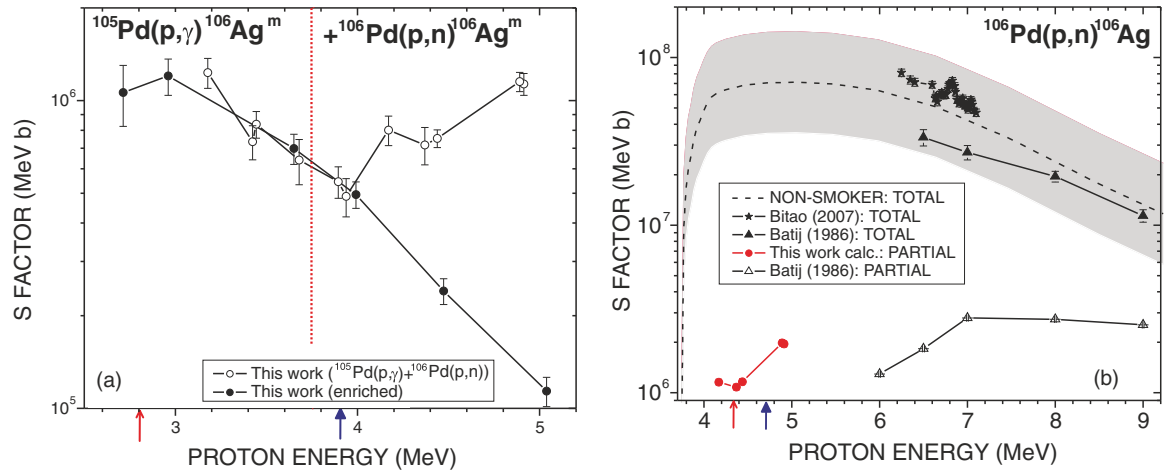

FIG. 7. (Color online) (a) S factors for ^{105}Pd$(p,\gamma)^{106}$Ag^m. The ^{106}Pd$(p,n)^{106}$Ag^m channel contributes above 3.78 MeV. (b) Decomposed S factor for ^{106}Pd$(p,n)^{106}$Ag^m in comparison with experimental data from Refs. [39] and [44]. The ^{106}Pd$(p,n)^{106}$Ag threshold is indicated as horizontal red line. The prediction from NON-SMOKER [36,37] (dashed line) is shown with a region of uncertainty of a factor of 2. The thin and thick arrows indicate the upper ends of the respective Gamow windows for $T = 2$ and 3 GK, respectively (see Table I).

E. ^{110}Pd$(p,n)^{110}$Ag^m

Activation of ^{110}Pd provided only the partial (p,n) cross section to the isomeric state in ^{110}Ag, which was measured via the γ lines at 657.8, 763.9, 884.7, and 937.5 keV in the decay of ^{110}Ag^m. The ground state of ^{110}Ag is too short lived for the technique used in this work ($t_{1/2} = 24$ s), and the NON-SMOKER calculation for the competing ^{110}Pd(p,γ) channel predicts a 1000 times lower cross section. Moreover, such events are difficult to detect because the strongest transition at 342.1 keV interferes with the strong 344.5-keV transition in ^{105}Ag ($t_{1/2} =$ 41.29 d).

The results for the cross section and the S factor are summarized in Table XIV. The comparison in Fig. 8 shows fair agreement (within ∼25%) with the measurement of Batij *et al.* [39] between 6 and 9 MeV. The total (p,n) data of Batij *et al.* [39] and Johnson *et al.* [45] are included for illustrating the measured energy trends with respect to the NON-SMOKER prediction. While the present results for the partial data follow the predicted slope, the total S factor of Johnson *et al.* exhibits increasing deviations toward lower energies.

TABLE XIII. Decomposed cross sections and S factors for the ^{106}Pd$(p,n)^{106}$Ag^m reaction, obtained with our experimental results from ^{105}Pd$(p,\gamma)^{106}$Ag^m.

E^{eff} (MeV)	Cross section (μb)	S factor (10^6 MeV b)
$4.170^{+0.027}_{-0.029}$	63.9 ± 7.0	1.15 ± 0.13
$4.370^{+0.028}_{-0.029}$	95.4 ± 13.3	1.08 ± 0.15
$4.438^{+0.025}_{-0.031}$	121 ± 8	1.17 ± 0.08
$4.890^{+0.030}_{-0.031}$	514 ± 37	1.98 ± 0.14
$4.913^{+0.028}_{-0.031}$	528 ± 43	1.95 ± 0.16

V. SUMMARY

Extensive investigationsof proton-induced reactions on Pd isotopes have been performed by means of the activation technique. The proton energy range between 2.7 and 8.8 MeV was chosen to cover relevant parts of the Gamow windows of the p process. Total cross sections are reported for ^{102}Pd$(p,\gamma)^{103}$Ag, ^{104}Pd$(p,\gamma)^{105}$Ag, and ^{105}Pd$(p,n)^{105}$Ag. In addition, partial cross sections were determined for the reactions ^{104}Pd$(p,n)^{104}$Ag^g, ^{105}Pd$(p,\gamma)^{106}$Ag^m, ^{106}Pd$(p,n)^{106}$Ag^m, and ^{110}Pd$(p,n)^{110}$Ag^m. Compared to previous experimental data, the present results for ^{102}Pd$(p,\gamma)^{103}$Ag are three times lower than those reported by Özkan *et al.* [38], whereas fair agreement was found with the ^{104}Pd$(p,\gamma)^{105}$Ag data of Spyrou *et al.* [43]. For the partial (p,n) cross sections measured in this work,

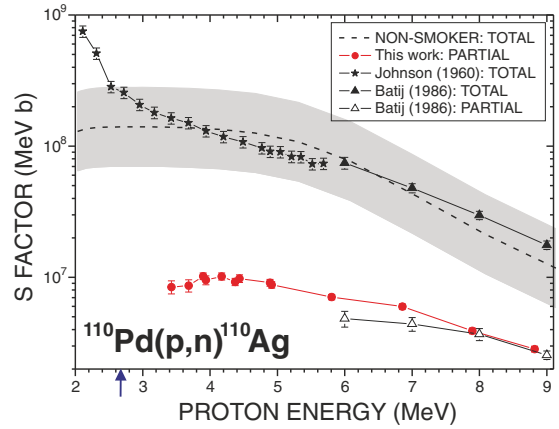

FIG. 8. (Color online) S factors for ^{110}Pd$(p,n)^{110}$Ag compared to the results of Johnson *et al.* [45] (stars) and Batij *et al.* [39] (open and full triangles) for the total and partial cross sections. The NON-SMOKER predictions [36,37] (dashed line) are plotted with a region of uncertainty of a factor of 2. The blue arrow indicates the upper end of the respective Gamow window for $T = 3$ GK (see Table I).

TABLE XIV. Cross sections and S factors for ^{110}Pd$(p,n)^{110}$Ag^m.

E^{eff} (MeV)	Cross section (mb)	S factor (10^6 MeV b)
$3.426^{+0.011}_{-0.016}$	0.058 ± 0.007	8.45 ± 0.98
$3.682^{+0.025}_{-0.029}$	0.131 ± 0.014	8.66 ± 0.93
$3.898^{+0.025}_{-0.029}$	0.282 ± 0.016	10.2 ± 0.58
$3.937^{+0.026}_{-0.029}$	0.293 ± 0.023	9.53 ± 0.75
$4.172^{+0.027}_{-0.029}$	0.566 ± 0.035	10.2 ± 0.63
$4.372^{+0.028}_{-0.029}$	0.819 ± 0.052	9.23 ± 0.59
$4.439^{+0.027}_{-0.031}$	1.01 ± 0.07	9.77 ± 0.67
$4.892^{+0.030}_{-0.030}$	2.36 ± 0.14	9.10 ± 0.55
$4.916^{+0.027}_{-0.032}$	2.38 ± 0.13	8.77 ± 0.50
$5.805^{+0.031}_{-0.034}$	8.29 ± 0.38	7.08 ± 0.33
$6.856^{+0.035}_{-0.037}$	26.7 ± 1.2	5.99 ± 0.26
$7.896^{+0.039}_{-0.040}$	49.1 ± 2.1	3.90 ± 0.17
$8.820^{+0.041}_{-0.043}$	76.2 ± 2.7	2.84 ± 0.10

we find only in the case of ^{110}Pd$(p,n)^{110}$Ag^m a reasonable agreement with the measured data of Batij *et al.* [39].

With respect to theory, the NON-SMOKER predictions [36,37] for ^{102}Pd(p,γ), ^{104}Pd(p,γ), and ^{105}Pd(p,n) were confirmed. These results confirm also the overall good agreement of NON-SMOKER calculations for proton-induced reactions of isotopes between ^{70}Ge and ^{209}Bi in the energy range of the Gamow window of the p process. From the 34 measured (p,γ) reactions so far, only ^{98}Ru, ^{114,116,119}Sn, and ^{115}In do not agree with NON-SMOKER within a factor-of-2 uncertainty. In the cases of ^{98}Ru and ^{115}In this seems to be solely due to experimental problems. For (p,n) reactions many more data are available within the Gamow window (datasets for 80 isotopes). A systematic comparison has not yet been carried out, but will be done in the p-process database of the "Karlsruhe Astrophysical Database of Nucleosynthesis in Stars" project [46].

The new reaction code SMARAGD [47] will be used for future predictions of astrophysical reaction rates. For the reactions investigated here, the predictions of the current version SMARAGD v0.8.1s with standard settings are identical to the shown NON-SMOKER results.

ACKNOWLEDGMENTS

We thank the operating team O. Döhr, H. Eggestein, T. Heldt, and M. Hoffmann for providing excellent beams at the PTB accelerators and W. Mannhart for providing a second HPGe at the PTB. I.D. acknowledges the help of M. Guttmann (Institut für Materialforschung, IMF) and A. Görtzen (Institut für Nukleare Entsorgung, INE), both from Forschungszentrum Karlsruhe (now Karlsruhe Institute of Technology, KIT), with an electrolytic cell. I.D. is funded by the Helmholtz association via the Young Investigators project VH-NG-627. This work was partially supported by the Swiss National Science Foundation (Grant No. 2000-113984/1). T.R. is supported by the European Commission within the FP7 ENSAR/THEXO project. F.-K.T. thanks the Alexander von Humboldt Foundation for support.

[1] E. Burbidge, G. Burbidge, W. Fowler, and F. Hoyle, Rev. Mod. Phys. **29**, 547 (1957).
[2] K. Langanke and M. Wiescher, Rep. Prog. Phys. **64**, 1657 (2001).
[3] S. Woosley and W. Howard, Astrophys. J. Suppl. **36**, 285 (1978).
[4] S. Woosley and W. Howard, Astrophys. J. **354**, L21 (1990).
[5] M. Rayet, M. Arnould, M. Hashimoto, N. Prantzos, and K. Nomoto, Astron. Astrophys. **298**, 517(R) (1995).
[6] T. Rauscher, A. Heger, R. Hoffman, and S. Woosley, Astrophys. J. **576**, 323 (2002).
[7] S. Woosley, D. Hartmann, R. Hoffman, and W. Haxton, Astrophys. J. **356**, 272 (1990).
[8] A. Heger, E. Kolbe, W. C. Haxton, K. Langanke, G. Martínez-Pinedo, and S. E. Woosley, Phys. Lett. B **606**, 258 (2005).
[9] M. Rayet, M. Arnould, and N. Prantzos, Astron. Astrophys. **227**, 271 (1990).
[10] T. Rauscher, F.-K. Thielemann, and H. Oberhummer, Astrophys. J. **451**, L37 (1995).
[11] W. Howard, B. Meyer, and S. Woosley, Astrophys. J. **373**, L5 (1991).
[12] S. Goriely, J. José, M. Hernanz, M. Rayet, and M. Arnould, Astron. Astrophys. **383**, L27 (2002).
[13] H. Schatz, A. Aprahamian, J. Görres, M. Wiescher, T. Rauscher, J. Rembges, F.-K. Thielemann, B. Pfeiffer, P. Möller, H. Herndl *et al.*, Phys. Rep. **294**, 167 (1998).
[14] H. Schatz, A. Aprahamian, V. Barnard, L. Bildsten, A. Cumming, M. Ouellette, T. Rauscher, F.-K. Thielemann, and M. Wiescher, Phys. Rev. Lett. **86**, 3471 (2001).
[15] C. Fröhlich, G. Martínez-Pinedo, M. Liebendörfer, F.-K. Thielemann, E. Bravo, W. R. Hix, K. Langanke, and N. T. Zinner, Phys. Rev. Lett. **96**, 142502 (2006).
[16] N. Dauphas, T. Rauscher, B. Marty, and L. Reisberg, Nucl. Phys. A **719**, 287c (2003).
[17] T. Rauscher, Phys. Rev. C **81**, 045807 (2010).
[18] T. Rauscher, Phys. Rev. C **73**, 015804 (2006).
[19] G. G. Kiss, T. Rauscher, G. Gyürky, A. Simon, Z. Fülöp, and E. Somorjai, Phys. Rev. Lett. **101**, 191101 (2008).
[20] T. Rauscher, G. G. Kiss, G. Gyürky, A. Simon, Z. Fülöp, and E. Somorjai, Phys. Rev. C **80**, 035801 (2009).
[21] C. Iliadis, *Nuclear Physics of Stars* (Wiley-VCH, Weinheim, 2007).
[22] H. Utsunomiya, P. Mohr, A. Zilges, and M. Rayet, Nucl. Phys. A **777**, 459 (2006).
[23] W. Rapp, J. Görres, M. Wiescher, H. Schatz, and F. Käppeler, Astrophys. J. **653**, 474 (2006).
[24] H. J. Brede, M. Cosack, G. Dietze, H. Gumpert, S. Guldbakke, R. Jahr, M. Kutscha, D. Schlegel-Bickmann, and H. Schölermann, Nucl. Instrum. Methods **169**, 349 (1980).
[25] N. Trautmann and H. Folger, Nucl. Instrum. Meth. A **282**, 102 (1989).
[26] J. De Laeter, J. Böhlke, P. de Bievre, H. Hidaka, H. Peiser, K. Rosman, and P. Taylor, Pure Appl. Chem. **75**, 683 (2003).
[27] R. Böttger (private communication).
[28] J. F. Ziegler and J. P. Biersack, The stopping and range of ions in matter, SRIM-2003.26 computer code [http://www.srim.org] (2003).

[29] H. Beer and F. Käppeler, Phys. Rev. C **21**, 534 (1980).
[30] D. de Frenne and E. Jacobs, Nucl. Data Sheets **93**, 447 (2001).
[31] J. Blachot, Nucl. Data Sheets **108**, 2035 (2007).
[32] D. de Frenne and E. Jacobs, Nucl. Data Sheets **105**, 775 (2005).
[33] D. de Frenne and A. Negret, Nucl. Data Sheets **109**, 943 (2008).
[34] D. de Frenne and E. Jacobs, Nucl. Data Sheets **89**, 481 (2000).
[35] K. Debertin and R. Helmer, *Gamma- and X-Ray Spectrometry With Semiconductor Detectors* (North-Holland, Amsterdam, 1989).
[36] T. Rauscher and F.-K. Thielemann, At. Data Nucl. Data Tables **75**, 1 (2000).
[37] T. Rauscher and F.-K. Thielemann, At. Data Nucl. Data Tables **79**, 47 (2001).
[38] N. Özkan, A. Murphy, R. Boyd, A. Cole, M. Famiano, R. Güray, M. Howard, L. Sahin, J. Zach, R. deHaan *et al.*, Nucl. Phys. A **710**, 469 (2002).
[39] V. Batij, E. Skakun, J. Rakivnenko, and O. Rastrepin, Proceedings of the 36th Conference on Nuclear Spectroscopy and Nuclear Structures, Kharkov, USSR (1986), p. 280.
[40] A. Lejeune, Phys. Rev. C **21**, 1107 (1980).
[41] Experimental Nuclear Reaction Data EXFOR, [http://www-nds.iaea.org/exfor/exfor.htm] (2009).
[42] H. Bitao, P. Zarubin, and U. Juralev, Eur. Phys. J. A **2**, 143 (1998).
[43] A. Spyrou, A. Lagoyannis, P. Demetriou, S. Harissopulos, and H. W. Becker, Phys. Rev. C **77**, 065801 (2008).
[44] H. Bi-Tao, P. Zarubin, and U. Juralev, Chin. Phys. **16**, 989 (2007).
[45] C. Johnson, A. Galonsky, and C. Inskeep, Oak Ridge National Laboratory Report No. ORNL-2910, 1960, p. 25 (unpublished).
[46] T. Szücs, I. Dillmann, R. Plag, and Z. Fülöp, 11th Symposium on Nuclei in the Cosmos, Proceedings of Science, PoS(NIC XI)247 (2011). Online published at [http://pos.sissa.it].
[47] T. Rauscher, Int. J. Mod. Phys. E **20**, 1071 (2011).